Available online at www.sciencedirect.com
ScienceDirect
Trans. Nonferrous Met. Soc. China 31(2021) 1217−1234
Transactions of Nonferrous Metals Society of China
www.tnmsc.cn

A unified constitutive model for multiphase precipitation and multi-stage creep ageing behavior of Al−Li−S4 alloy

He LI[1], Li-hua ZHAN[1,2,3], Ming-hui HUANG[1,2,3], Xing ZHAO[1,2,3], Chang ZHOU[2], Li-bin HU[2], Zheng-gen HU[2,4], De-bo LIU[4]

1. Light Alloy Research Institute, Central South University, Changsha 410083, China;
2. School of Mechanical and Electrical Engineering, Central South University, Changsha 410083, China;
3. State Key Laboratory of High-Performance Complex Manufacturing, Central South University, Changsha 410083, China;
4. Beijing Institute of Astronautic Systems Engineering, Beijing 100076, China

Received 2 May 2020; accepted 4 February 2021

Abstract: A unified constitutive model is presented to predict the recently observed "multi-stage" creep behavior of Al−Li−S4 alloy. The corresponding microstructural variables related to the yield strength and creep deformation of the alloy during the creep ageing process, including dislocations and multiple precipitates, have been characterized in detail by X-ray diffraction (XRD) and transmission electron microscopy (TEM). For the yield strength, the model considers the multiphase strengthening behavior of the alloy based on strengthening mechanisms, which includes shearable T_1 precipitate strengthening, non-shearable T_1 precipitate strengthening and θ' precipitate strengthening. Based on creep deformation mechanism, the "multi-stage" creep behavior of the alloy is predicted by introducing the effects of interacting microstructural variables, including the radius of multiple precipitates, dislocation density and solute concentration, into the creep stress−strain model. It is concluded that the results calculated by the model are in a good agreement with the experimental data, which validates the proposed model.

Key words: constitutive modelling; Al−Li−S4 alloy; creep age forming; microstructures; numerical algorithms

1 Introduction

Creep age forming is an advanced metal forming technique originally developed to manufacture large aluminum components in aircraft and aerospace industry [1]. This method utilizes the heating and pressurizing capabilities of an autoclave in combination with special tools to exploit the basic creep phenomenon that occurs during the artificial ageing of metals [2]. In order to significantly improve the forming accuracy and mechanical performance of large complex components, the creep age forming (CAF) process has been widely studied in recent years [3−6]. During the CAF process, stress-induced deformation and artificial ageing occur simultaneously and interact with each other. This process determines the springback and mechanical properties of the formed components. Recent experiments revealed the "multi-stage" creep behavior of Al−Li−S4 alloys. Therefore, it is important to establish a constitutive model to predict the creep ageing behavior affected by various types of precipitates.

Precipitation hardened Al−Cu−Li alloys have excellent properties such as low density, high specific rigidity, high elastic modulus, high specific

Corresponding author: Li-hua ZHAN, E-mail: yjs-cast@csu.edu.cn;
Xing ZHAO, Tel: +86-731-88877856, E-mail: xingzhao@csu.edu.cn
DOI: 10.1016/S1003-6326(21)65573-5

strength, good fatigue, good corrosion resistance and sound weldability [7,8]. Therefore, they have been widely used to manufacture structural components in the aerospace industry [7,9]. Al−Li−S4 alloy, the newest third generation Al−Li alloy launched by Alcoa Inc. in 2011, has been used in thin-walled components such as fuselage and lower wings [10]. The Al−Cu−Li alloys with the major solute elements of Cu and Li and minor solute additions of Mg and Ag show a complicated precipitation sequence [11]. The binary Al−Cu system involves Guinier−Preston (GP) zones, θ'' and θ'. The Al−Li system forms the δ' precipitate with the nominal composition of Al_3Li. The tertiary system generates the main strengthening T_1 precipitate with the nominal composition of Al_2CuLi, which forms thin platelets on {111} planes of the Al matrix. The T_1 precipitate was initially thought to be hardly shearable. However, recent experiments revealed that the T_1 precipitate can be sheared by dislocation [12]. Therefore, the contribution of T_1 precipitate to the strength of the alloy should be divided into shearable and non-shearable parts.

In recent decades, the constitutive modelling of the CAF process involving creep deformation and strengthening mechanisms has attracted extensive attentions. Many age hardening and creep damage variables were introduced to precisely predict the creep behavior during CAF process. KOWALEWSKI et al [13] developed a creep constitutive model by introducing two variables for the damage caused by creep cavitation and overaging. They showed that the developed equations can accurately describe the strain rate and fracture behavior in a narrow stress range. HO et al [14] established a unified creep ageing constitutive model, which could simultaneously demonstrate creep deformation and age-hardening behavior of Al alloys. With the increasing understanding of the microstructural evolution of Al alloys during the CAF process, some of the newly established creep constitutive models have made remarkable improvements in modeling the evolution of microstructures and yield strength of Al alloys. LI et al [15] developed a unified creep-ageing constitutive model for the 7B04 Al alloy, which investigated the effects of the relative volume fraction and the mean radius of precipitates on the creep rate and yield strength. ZHAN et al [16] recently proposed a unified creep ageing constitutive equation, which can simulate the evolution of precipitates, dislocation hardening, solid solution hardening and precipitation hardening and yield strength of Al alloys during the CAF process. The obtained simulation results were in good agreement with the experimental data. LI et al [17] introduced the interactions among precipitates, solutes and dislocations. Moreover, they presented the concepts of the threshold stress to construct a unified constitutive model for asymmetric tensile and compressive creep ageing behavior of the Al−Cu−Li alloy (AA2050). They also accurately described the evolutions of the average diameter of T_1 precipitates, yield strength and creep rate. Moreover, some of the models were successfully implemented into the finite element software to model the forming behavior and springback of components during the CAF process [18−20].

The existing models mainly consider the total effect of the precipitation strengthening on yield strength. However, there are few reports on the constitutive model that can describe the creep rate, strength and microstructure evolution of Al−Cu−Li alloys with multiphase under different stress levels. In the present study, a unified creep ageing constitutive model for Al−Li−S4 alloy under different stress levels is developed, which can demonstrate the morphological evolution of T_1 and θ' phases.

2 Experimental

Table 1 presents the chemical compositions of the 2 mm-thick commercial Al−Li−S4 plate used in this study. Dog-bone-shaped tensile specimens were cut from the plate using an electrical discharge machine with the loading direction parallel to the rolling direction. Figure 1 shows the geometric dimensions of the specimen. The process diagram of the whole heat treatment and test conditions is shown in Fig. 2. Specifically, the samples were initially solution-treated in a resistance furnace at 530 °C for 80 min, and immediately water quenched. The temperature deviation of the furnace was less than 2 °C during solution treatment, and it took less than 20 s to carry samples from the furnace to the water tank. In order to reduce the effects of natural ageing, these samples were stored at −20 °C before creep tests.

Table 1 Chemical compositions of Al−Li−S4 aluminum alloy (wt.%)

Cu	Mg	Mn	Fe	Si
3.64	0.71	0.29	0.028	0.014
Zn	Zr	Li	Ti	Al
0.36	0.12	0.69	0.026	Bal.

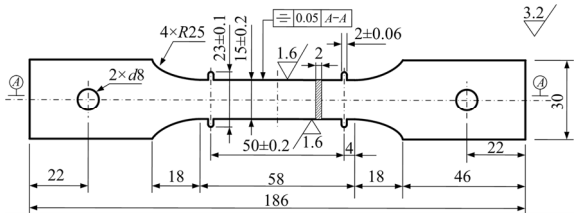

Fig. 1 Geometry of creep specimen (Unit: mm)

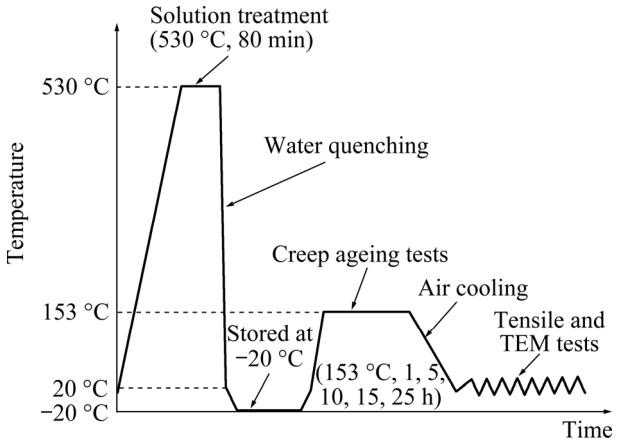

Fig. 2 Schematic diagram showing heat treatment and test conditions

Uniaxial tensile creep tests were carried out on an RDL50 creep machine equipped with a furnace, and the tests were carried out at 153 °C under constant stresses of 200, 220 and 240 MPa for 1, 5, 15, 20 and 25 h, respectively. The specimen was first heated to 153 °C at a heating rate of 4 °C/min, and kept for 10 min in resistance heating furnace. Then, the exterior stress was smoothly loaded at a rate of 15 N/s using computer-aided controlling system. When the experiment was finished, all specimens were cooled to room temperature in the air. Tensile tests were carried out using a DDL100 electronic testing machine at a strain rate of 2 mm/min at room temperature. Three tensile tests were performed to obtain an average value.

The microstructural evolution of Al−Li−S4 alloys was characterized by scanning transmission electron microscopy (STEM) and XRD. STEM samples were first mechanically thinned to 60−80 μm using metallographic sandpapers. Then, the samples were cut into 3 mm-diameter discs and finally thinned by the twin-jet electropolishing using a solution of 80% methanol and 20% nitric acid at approximately −25 °C, with a potential of 14 V. Aberration corrected high angle annular dark field (HAADF) TEM observations were carried out on a Tecnai-F20 operated at 200 kV. The XRD samples are cut from the middle part of the creep-aged samples by an electrical discharge machine and mechanically polished and thinned to the size of 5 mm × 5 mm × 1 mm. The XRD tests are conducted on an advance D8 X-ray diffractometer with a scan range (2θ) from 20° to 90° and a speed of 0.02° for each step. Three XRD tests are performed to obtain an average value of the peak full width at half maximum (FWHM).

3 Results

3.1 Creep behavior

Figure 3(a) shows the creep strain curves of Al−Li−S4 alloys at 153 °C under applied stresses of 200, 220 and 240 MPa for 25 h. The corresponding creep strain rate curves of the alloy are shown in Fig. 3(b). It is observed that all creep strain curves exhibit “multi-stage” behavior during the creep ageing (CA) process. According to the trend of creep strain rate during CA process [21], the creep strain curves demonstrate a special three-stage (I, II and III) phenomenon, including the first primary CA stage (Stage I), the first steady CA stage (Stage II), and the second primary CA stage (Stage III). It is worth noting that the creep rate of the alloy in Stage III tends to be constant, which is different from the traditional tertiary creep stage where the creep rate increases rapidly. More details of the experimental setup and results can be found in the study of MA et al [22]. The “multi-stage” creep feature is reported to be mainly controlled by the microstructural evolution, including dislocations, solutes and precipitates [21,22].

3.2 Dislocations density evolution during CA process

During the CA process, it is difficult to quantitatively analyze the dislocation density by TEM. In addition, some dislocations are easily interfered and covered by the precipitates [23]. According to the study of RODGERS and PRANGNELL [23] and UNGÁR et al [24], the

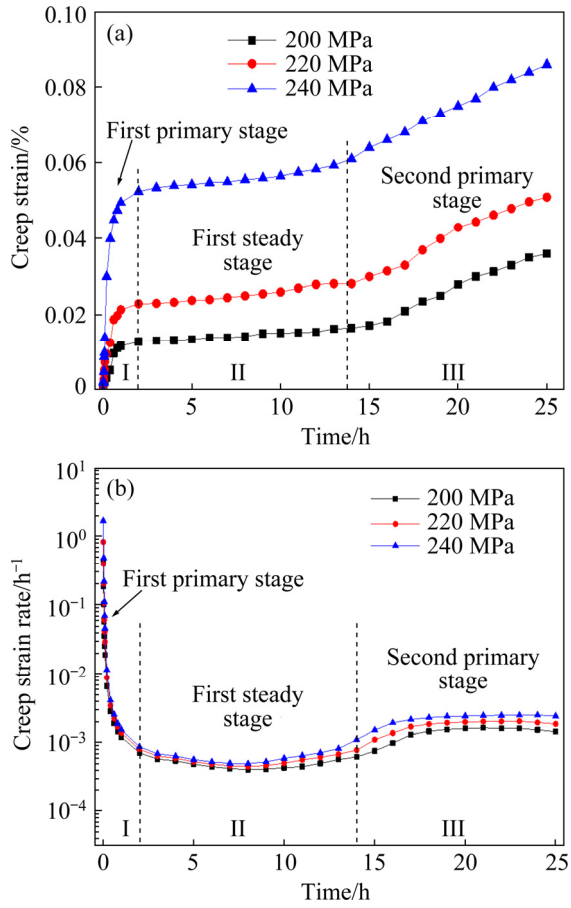

Fig. 3 Creep strain curves (a) and creep strain rate curves (b) of Al−Li−S4 alloy under different applied stresses at 153 °C for 25 h

dislocation density can be calculated by the modified Williamson−Hall plot, which is mathematically described as Eq. (1):

$$\Delta K \approx 0.9/D_a + (\pi M^2 b^2/2)^{1/2} \rho^{1/2} K \bar{C}^{1/2} \quad (1)$$

$$K = 2\sin\theta/\lambda \quad (2)$$

$$\Delta K = 2\cos\theta \cdot \Delta\theta/\lambda \quad (3)$$

where D_a is the average grain size, M is a constant depending on the effective outer cut-off radius of dislocations, b is the magnitude of Burgers vector (0.286 nm for aluminium), ρ is the dislocation density, θ is the diffraction angle, λ is the wavelength of X-rays, $\Delta\theta$ is the full width at half maximum (FWHM), K is the diffraction constant, ΔK is the strain broadened FWHM in the reciprocal space, and $\bar{C}$ is the average contrast factor for each particular plane (hkl) given by

$$\bar{C} = \bar{C}_{h00}(1 - qH^2) \quad (4)$$

where H^2 and $\bar{C}_{h00}$ denote the fourth-order ratio and the average contrast factor corresponding to the (h00) reflection, respectively. Moreover, q represents different broadening anisotropies, and its value depends on whether dislocations are edge or screw in the character [24,25]. It is worth noting that the value of $\bar{C}_{h00}$ can vary significantly between the edge and screw dislocations. In order to simplify the algorithm, it is assumed that the distribution of both edge dislocations and screw dislocations is uniform. According to the study of UNGÁR et al [24], the average values of $\bar{C}_{h00}$ and q are 0.40 and 2.3369, respectively.

According to the study of WILLIAMSON and HALL [26], the quadratic form of the modified Williamson−Hall plot was written as

$$(\Delta K)^2 \approx (0.9/D_a)^2 + (\pi M^2 b^2/2)\rho K^2 \bar{C} \pm O(K^4 C^2) \quad (5)$$

where $O(K^4C^2)$ denotes non-interpreted higher-order term. Substituting Eq. (4) into Eq. (5) yields

$$\frac{\Delta K^2 - \alpha}{K^2} \approx \beta \bar{C}_{h00}(1 - qH^2) \quad (6)$$

$$\rho = \frac{2\beta}{\pi M^2 b^2} \quad (7)$$

where $\alpha = (0.9/D_a)^2$ and $\beta = \pi M^2 b^2 \rho/2$. The value of $\beta\bar{C}_{h00}$ can be determined by the linear regression of $(\Delta K^2 - \alpha)/K^2$ versus H^2.

Figure 4(a) presents the X-ray diffraction curves of the selected samples under 220 MPa for 0 h and under 240 MPa for 0, 1, 5, 15 and 25 h, respectively. Moreover, it is found that the diffraction peaks of T_1 and θ' phases increase gradually during the CA process, which indicates that T_1 and θ' precipitates nucleate and grow gradually. The XRD spectra of Al−Li−S4 alloy are analyzed with the JADE software to obtain the value of FWHM and the diffraction angle θ. The parameters of α and $\beta\bar{C}_{h00}$ corresponding to the five diffraction peaks of each X-ray diffraction curve are fitted by the least square method. Furthermore, the value of the dislocation density ρ is calculated by Eq. (7). Figures 4(b−d) show the values of α, $\beta\bar{C}_{h00}$ and ρ, respectively. Three XRD tests are performed to obtain an average value. As shown in Fig. 4(d), dislocation density of the selected samples under 240 MPa increases rapidly at 1 h and decreases significantly from 5 to 15 h. Then, the dislocation density decreases slightly until the end of the CA process. Besides, when the

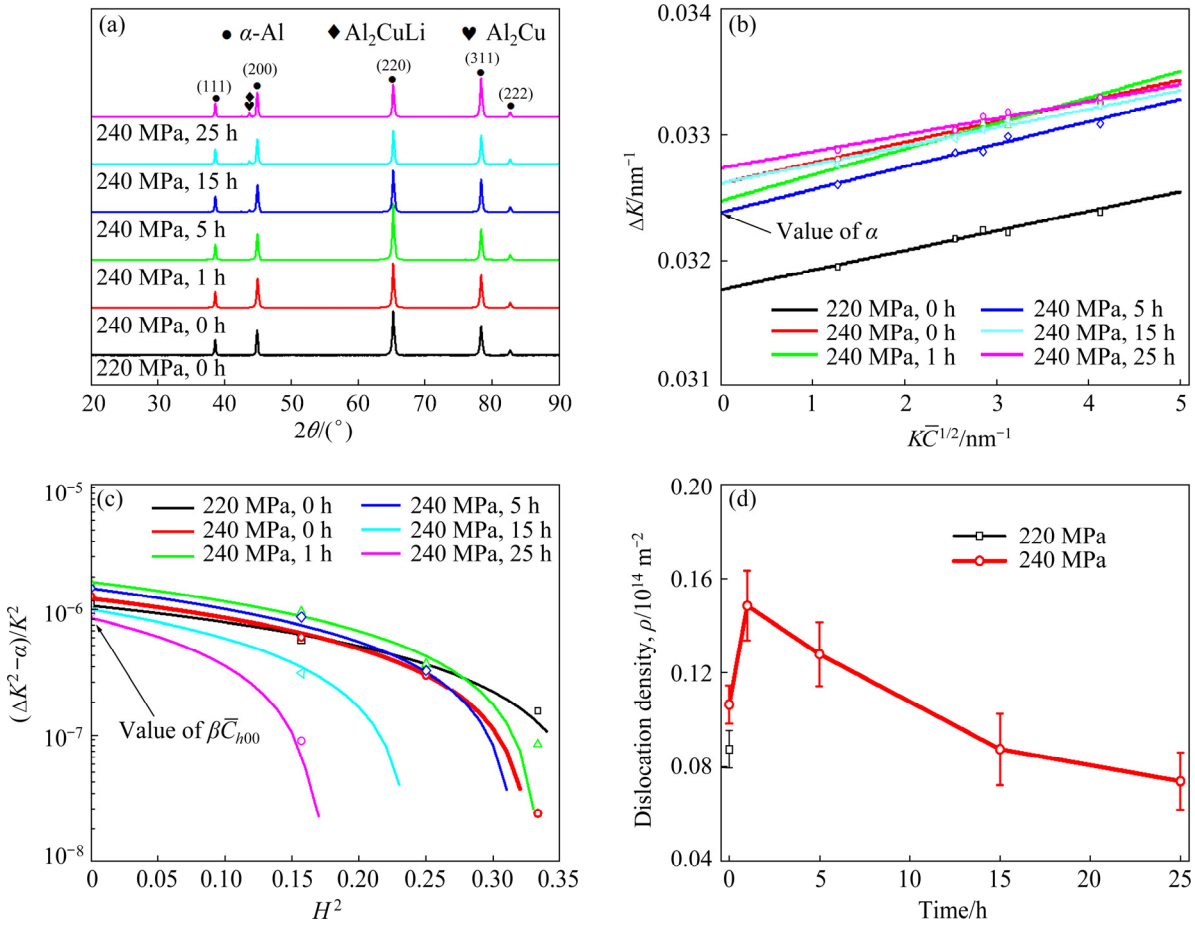

Fig. 4 X-ray diffraction patterns of Al−Li−S4 alloy under different stresses for different time (a), value of α from Eq. (1) (b), value of $\beta\overline{C}_{h00}$ from Eq. (6) (c), and dislocation density ρ according to Eq. (7) (d)

applied stress is 240 MPa, 0.65% plastic deformation is generated in the sample, which increases the dislocation density of the sample. Therefore, the initial dislocation density of the specimen under 220 MPa is lower than that under 240 MPa.

3.3 Precipitates evolution

Figures 5(a, b) show TEM images of the distributions of T_1 and θ' precipitates of the selected samples under 240 MPa at 153 °C for 5 and 25 h, respectively. It should be indicated that all images were taken along ⟨110⟩ matrix zone axis. There are four variants of T_1 precipitate lying on the $\{111\}_{\text{Matrix}}$ planes and three variants of θ' precipitate lying on the $\{100\}_{\text{Matrix}}$ planes. Under the TEM observation along the ⟨110⟩ matrix zone axis of Al matrix, two variants of the T_1 precipitate and one variant of θ' precipitate are in the edge-on configuration. The angle between the two variants of T_1 precipitate is 109.4° and the variant of the θ' precipitate is on the angle bisector of the two variants of T_1 precipitate. Furthermore, the crystallographic orientations are indicated at the upper right of each graph, which was also demonstrated in an earlier study [22]. It can be seen from Fig. 5 that T_1 and θ' precipitates play an important role in the strengthening behavior of the alloy during the CA process.

Figure 6 presents the HAADF-STEM images of Al−Li−S4 alloys taken along ⟨100⟩ matrix zone axis. All samples in Figs. 6(a−d) are aged at 153 °C under 240 MPa for 1, 5, 15 and 25 h, respectively. Figure 6(a) shows that the matrices are very pure without any precipitates. Moreover, it is found that a large number of dislocations caused by the plastic deformation during the creep loading stage distribute uniformly in the matrices. In Fig. 6(b), a small quantity of θ' precipitates appear in the crystal. In Fig. 6(c), a large number of θ' precipitates are generated along with a close-packed $\{001\}_{\text{Matrix}}$ habit plane and distribute uniformly. In Fig. 6(d), the size and number of θ' phases are reduced compared with those of the alloy aged for 15 h,

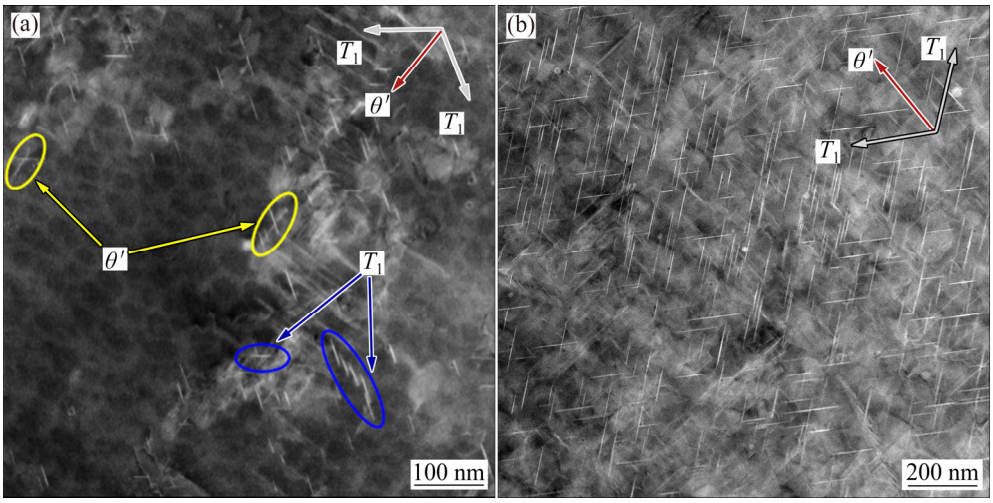

Fig. 5 HAADF-STEM images of Al−Li−S4 alloy during CA process under stress of 240 MPa for 5 h (a) and 25 h (b) (All images were taken along ⟨110⟩ matrix zone axis)

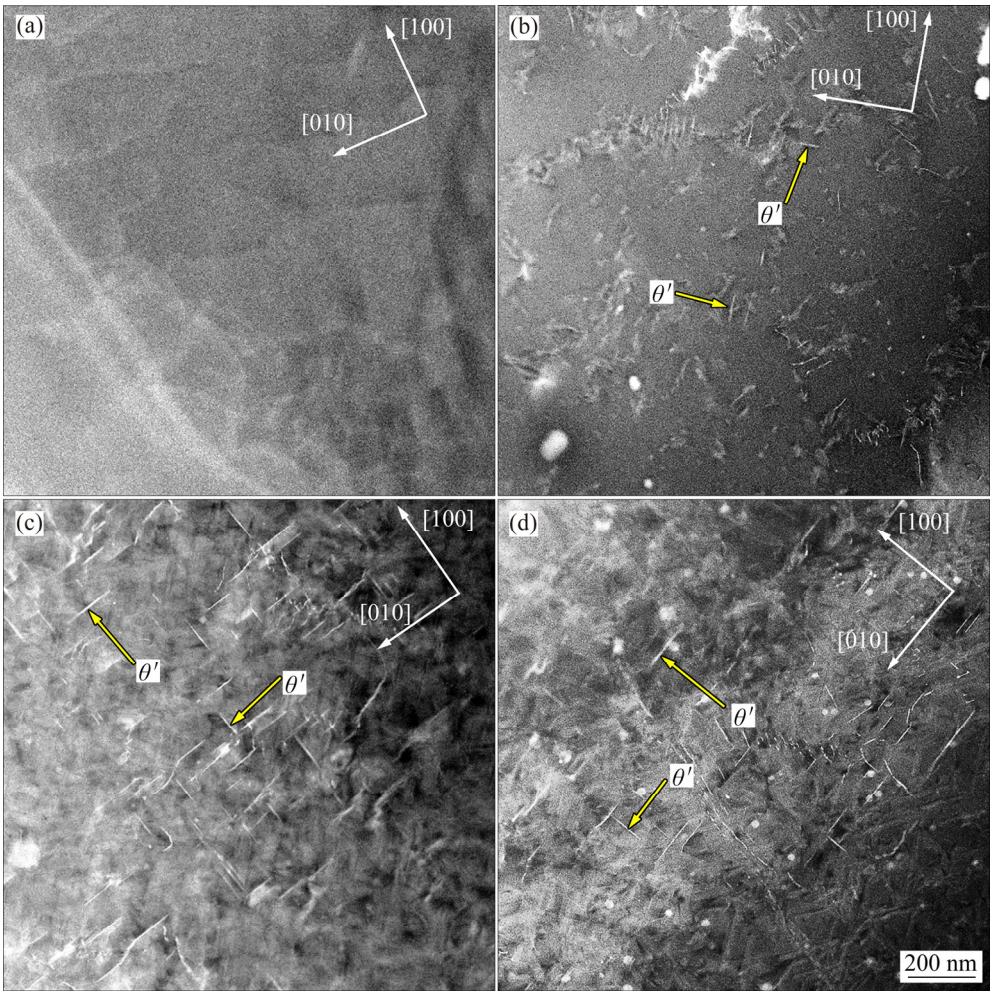

Fig. 6 TEM images of selected specimens under stress of 240 MPa at 153 °C for 1 h (a), 5 h (b), 15 h (c) and 25 h (d) (All images were taken along ⟨100⟩ matrix zone axis)

which is also consistent with the results reported about Al−Cu−Li alloys [27]. According to RODGERS and PRANGNELL [23], the higher the dislocation density is, the more homogenously the T_1 precipitates distribute, and the higher the volume fraction of T_1 precipitate is. When T_1 precipitates

nucleate and grow up, the formation of T_1 precipitates consumes much Li and Cu atoms, thereby reducing θ' precipitates.

4 Constitutive modelling

In the present study, a unified creep ageing constitutive model is developed for the analysis and simulation of the correlation between material properties and corresponding microstructural variables of the aluminum alloy. There are many kinds of precipitates in Al−Li−S4 alloy, including T_1, θ' and δ' phases. Compared with the single kind of precipitate of 2219 aluminum alloy [28], the evolution of microstructures of Al−Li−S4 alloy during the CA process is more complicated. In order to accurately describe the creep deformation and ageing strengthening behavior of the alloy, the effects of the dislocation density ρ and two kinds of the main precipitates (T_1 and θ') on the creep ageing behavior are comprehensively considered in this study. For the purpose of simplification, the profiles of T_1 and θ' precipitates are in the same plate shape [17,28]. Figure 7 shows the corresponding geometrical model. In order to describe the variation law of the plate-shaped precipitates in the aluminum alloy, the necessary parameters are average diameter D, average thickness T and relative volume fraction f_v of the precipitate.

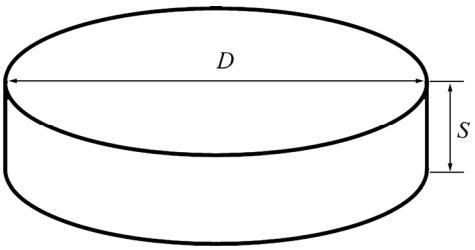

Fig. 7 Geometrical model for plate-shaped T_1 and θ' precipitates

4.1 Model for dislocation density evolution

It should be indicated that dislocation movement generally dominates the plastic deformation. Therefore, the evolution of dislocation density plays a key role in the creep behavior during the CA process. The evolution of the dislocation density ρ during the CA process is determined by two parts, including the dislocation accumulated before the CA process ρ_i and the dislocation developed with the creep deformation ρ_c, which can be expressed with Eq. (8) [17]:

$$\rho=\rho_i+\rho_c \tag{8}$$

A number of dislocations can be initially produced during the loading stage when the applied stress is higher than the initial yield strength of the material. The dislocation density ρ_i generated before the CA process can be divided into two parts, including dislocations generated by quenching and the applied stress during the loading stage. The dislocation density can be expressed as [29]

$$\rho_i=\rho_0+c_{17}\exp[c_{18}(1+(\sigma-\sigma_{0.2})/\sigma_{0.2})] \tag{9}$$

$$\overline{\rho}=\rho_i/\rho_{total} \tag{10}$$

where c_{17} and c_{18} are the material-related constants. $\sigma_{0.2}$ and ρ_0 denote the initial yield strength of the material before the loading stage and the dislocation density caused by quenching, respectively. It should be indicated that ρ_0 is assumed to be 0.05×10^{14} m^{-2}. Dislocation density $\overline{\rho}_i$ is normalized by dividing ρ_i by ρ_{total} in Eq. (10). ρ_{total} is the saturated dislocation density. According to the study of LI et al [21], there is a limit of the pre-stretch level. Above this limit, the age hardening progress would be hardly affected by further increasing pre-stretch levels. More specifically, for the Al−2.45Cu−2.45Li alloy, the limit is about 6%. For the sake of simplicity, its value is equal to the dislocation density generated by the 6% pre-deformation (0.43×10^{14} m^{-2}).

The evolution of the dislocation density during the CA process is determined by two factors, including the dislocation multiplication caused by creep deformation and dynamic recovery during the CA stage at relatively high temperature [16]. The evolution of the dislocation density has been modelled in many previous publications [17,29]. Moreover, its rate can be described as

$$\dot{\overline{\rho}}_c=c_{19}(1-\overline{\rho})|\dot{\varepsilon}_c|^{m_{13}}-c_{20}\overline{\rho}^{n_{13}} \tag{11}$$

where c_{19}, c_{20}, m_{13} and n_{13} are the material-related constants, and $\dot{\varepsilon}_c$ is the creep rate. Equation (11) is composed of two parts. The first part of $c_{19}(1-\overline{\rho})|\dot{\varepsilon}_c|^{m_{13}}$ means dislocation multiplication caused by the creep deformation, and $\overline{\rho}_c$ is the normalized dislocation density in the CA process. The second part of $-c_{20}\overline{\rho}^{n_{13}}$ denotes the dislocation dynamic recovery.

4.2 Model for precipitate growth

For the multiple types of precipitate distribution of Al−Li−S4 alloys, the T_1/θ'

competition during the CA process should be considered at different applied stress levels. As discussed before, the growth of both θ' and T_1 phases consumes Cu atoms in the Al matrix, while T_1 precipitation continues consuming θ' during the CA process [27]. Moreover, there are two types of T_1 precipitates, including shearable and non-shearable ones, which affect the mechanical properties and creep behavior of the alloy. For the purpose of simplification, three assumptions are made: (1) In the CA process, T_1 precipitate with the thickness less than 3 nm is shearable, while it is non-shearable with the thickness greater than 3 nm [30]. (2) The volume fraction of plate-shaped T_1 and θ' precipitates under homogeneous nucleation satisfies the same evolution laws [17]. (3) The dissolved volume fraction of θ' precipitate is all converted to T_1 precipitate. Moreover, the non-shearable T_1 precipitate evolves from the shearable T_1 precipitate.

4.2.1 Relative volume fraction of T_1 and θ' precipitates

During the CA process, the supersaturated solute atoms are gradually consumed to form precipitates from the Al matrix [28]. According to the study of LIU et al [31], the volume fraction of plate-shaped T_1 and θ' precipitates under the homogeneous nucleation conditions can be mathematically expressed as

$$f_{\mathrm{v}}=\frac{\pi D^2 S}{4}RN_0Z\beta^*\exp\left(\frac{-\Delta G}{kT}\right)t \tag{12}$$

where D and S are average length and thickness of precipitates, respectively. R is the Avogadro number, N_0 is the number of mole by unit volume, Z is the Zeldovich's factor (≈0.05), β^* is material parameter, k is the Boltzmann constant, T is the ageing temperature, ΔG is the critical activation energy for precipitation, and t is the ageing time.

In order to simplify the modeling process, a more general parameter named the normalized volume fraction is introduced:

$$\begin{cases}\overline{f}_{\mathrm{v}}=f_{\mathrm{v}}/f_{\mathrm{v\text{-}max}}\\ \overline{f}_{\mathrm{v}}=f_{\mathrm{v\text{-}\theta'}}+f_{\mathrm{v\text{-}T}}\\ \dot{\overline{f}}_{\mathrm{v}}=\dot{\overline{f}}_{\mathrm{v\text{-}\theta'}}+\dot{\overline{f}}_{\mathrm{v\text{-}T}}\end{cases} \tag{13}$$

where f_{v} is the current absolute volume fraction of both T_1 and θ' precipitates. $f_{\mathrm{v\text{-}max}}$ is the maximum sum of the volume fraction of T_1 and θ' precipitates. $\dot{\overline{f}}_{\mathrm{v}}$, $\dot{\overline{f}}_{\mathrm{v\text{-}\theta'}}$ and $\dot{\overline{f}}_{\mathrm{v\text{-}T}}$ are corresponding current relative volume fraction rates of different precipitates, respectively. In the CA process, the parameter β^* and the activation energy ΔG of T_1 and θ' precipitates are different, which depends on temperature, ageing time, and dislocation density. According to the abovementioned data and relevant research of ZHANG et al [32], the evolution of the relative volume fraction of θ' precipitate can be expressed as

$$\dot{\overline{f}}_{\mathrm{v\text{-}\theta'}}=c_1\dot{D}_{\theta'}D_{\theta'}^2S_{\theta'}(1+k_6\overline{\rho}^{n_4})(1-\overline{f}_{\mathrm{v\text{-}\theta'}})^{m_3}-c_2\dot{\overline{f}}_{\mathrm{v\text{-}\theta'}}^{m_4} \tag{14}$$

where c_1, c_2, m_3, m_4, n_4 and k_6 are the material-related constants. $\dot{D}_{\theta'}$, $D_{\theta'}$ and $S_{\theta'}$ denote the average diameter evolution rate, the average diameter and average thickness evolution of θ' precipitate, respectively. The first term $c_1\dot{D}_{\theta'}D_{\theta'}^2S_{\theta'}(1+k_6\overline{\rho}^{n_4})(1-\overline{f}_{\mathrm{v\text{-}\theta'}})^{m_3}$ plays a dominant role in describing the increasing process of the relative volume fraction of the θ' precipitate, which leads to a decreasing rate with time. Moreover, the second term $-c_2\dot{\overline{f}}_{\mathrm{v\text{-}\theta'}}^{m_4}$ controls the dissolution process of the θ' precipitate, which can be transformed into the T_1 precipitate. According to the previous study of MA et al [29], the relative volume fraction of the shearable and non-shearable T_1 precipitates can be expressed as Eqs. (15) and (16), respectively:

$$\begin{aligned}\dot{\overline{f}}_{\mathrm{v\text{-}Ts}}=&c_3\dot{D}_{\mathrm{Ts}}D_{\mathrm{Ts}}^2S_{\mathrm{Ts}}(1+k_7\overline{\rho}^{n_5})(1-\overline{f}_{\mathrm{v\text{-}Ts}})^{m_5}+\\ &c_4c_2\dot{\overline{f}}_{\mathrm{v\text{-}\theta'}}^{m_4}-c_5\dot{\overline{f}}_{\mathrm{v\text{-}Ts}}^{m_6}\end{aligned} \tag{15}$$

$$\begin{aligned}\dot{\overline{f}}_{\mathrm{v\text{-}Tns}}=&[c_5\dot{\overline{f}}_{\mathrm{v\text{-}Ts}}^{m_6}+(1-c_4)c_2\dot{\overline{f}}_{\mathrm{v\text{-}\theta'}}^{m_4}]\cdot\\ &[1+c_6(1+k_8\overline{\rho}^{n_6})(1-\overline{f}_{\mathrm{v\text{-}Tns}})^{m_7}]\end{aligned} \tag{16}$$

where $c_{2\text{–}6}$, $m_{4\text{–}7}$, n_5, n_6, k_7 and k_8 are the material-related constants. $\dot{\overline{f}}_{\mathrm{v\text{-}Ts}}$ and $\dot{\overline{f}}_{\mathrm{v\text{-}Tns}}$ are the current relative volume fraction rates of the shearable and non-shearable T_1 precipitates, respectively. $\dot{D}_{\mathrm{Ts}}$ and $\dot{D}_{\mathrm{Tns}}$ are the average diameter evolution rates of the shearable and non-shearable T_1 precipitates, respectively. D_{Ts} and D_{Tns} are the average diameters of the shearable and non-shearable T_1 precipitates, respectively. S_{Ts} and S_{Tns} are the average thicknesses of the shearable and non-shearable T_1 precipitates, respectively. $c_4c_2\dot{\overline{f}}_{\mathrm{v\text{-}\theta'}}^{m_4}$ indicates the relative volume fraction rate of shearable T_1 precipitate transformed from θ' precipitate, and $-c_5\dot{\overline{f}}_{\mathrm{v\text{-}Ts}}^{m_6}$ represents the relative volume fraction rate of non-shearable T_1 precipitate

transformed from the shearable T_1 precipitate in Eq. (15). $c_5\dot{\overline{f}}_{\text{v-Ts}}^{m_6}$ is the relative evolution rate of the non-shearable T_1 precipitate, and $(1-c_4)c_2\dot{\overline{f}}_{\text{v-}\theta'}^{m_4}$ is the relative evolution rate of the non-shearable T_1 precipitate transformed from θ' precipitate.

4.2.2 Average length of T_1 and θ' precipitates

During the CAF process, the variation of the precipitate length depends mainly on the dislocation density, ageing temperature and time. As the temperature is constant during the CA process, the influence of temperature is not taken into account. However, the decrease of θ' average size caused by Cu atom transformed from θ' to T_1 should be considered. According to the researches [28,29], the evolution equation of the length of θ' precipitate can be expressed as

$$\dot{D}_{\theta'}=c_7(Q_1-D_{\theta'})^{m_8}(1+k_9\overline{\rho}^{n_7})-c_8[\overline{f}_{\text{v-}\theta'}/(1-c_9\overline{f}_{\text{v}})]^{m_9} \tag{17}$$

where c_{7-9}, m_8, m_9, n_7, k_9 and Q_1 are the material-related constants. The first term $c_7(Q_1-D_{\theta'})^{m_8}(1+k_9\overline{\rho}^{n_7})$ denotes the growth rate of the average length of θ' precipitate, and the second term $-c_8[\overline{f}_{\text{v-}\theta'}/(1-c_9\overline{f}_{\text{v}})]^{m_9}$ denotes the influence of the dissolution on the length evolution rate of θ' precipitate. Similarly, According to the study of YANG et al [28], the average length of the shearable and non-shearable T_1 precipitates can be expressed as Eqs. (18) and (19), respectively:

$$\dot{D}_{\text{Ts}}=c_{10}(Q_2-D_{\text{Ts}})^{m_{10}}(1+k_{10}\overline{\rho}^{n_8}) \tag{18}$$

$$\dot{D}_{\text{Tns}}=c_{11}(Q_3-D_{\text{Tns}})^{m_{11}}(1-k_{11}\overline{\rho}^{n_9}) \tag{19}$$

where c_{10}, c_{11}, m_{10}, m_{11}, n_8, n_9, k_{10}, k_{11}, Q_2 and Q_3 are the material-related constants. According to aforementioned data and relevant investigation of HU et al [33], during the CA process, the dislocation density in the material gradually increases as the creep stress increases, which gradually reduces the average length of the non-shearable T_1 precipitate. The second item on the right side of Eq. (19) $(1-k_{11}\overline{\rho}^{n_9})$ represents the influence of the dislocation on the growth of the non-shearable T_1 precipitate.

4.2.3 Average thickness of T_1 and θ' precipitates

Precipitate thickness is also an important parameter for precipitation hardening potential [29]. It should be indicated that during the isothermal CA process, the precipitate grows mainly by the volume diffusion mechanism. According to Fick's second law of diffusion, the growth rate of the precipitate thickness is proportional to the (−1/2) power of time. Considering the dissolution factor of θ' precipitate and the effect of the dislocation, and according to the study of MA et al [29], the thickness evolution of θ' precipitate can be expressed as

$$\dot{S}_{\theta'}=c_{12}t^{-1/2}(1+k_{12}\overline{\rho}^{n_{10}})-c_{13}[\overline{f}_{\text{v-}\theta'}/(1-c_{14}\overline{f}_{\text{v}})]^{m_{12}} \tag{20}$$

where c_{12-14}, m_{12}, n_{10} and k_{12} are the material-related constants. $\dot{S}_{\theta'}$ is the average thickness rate evolution of θ' precipitate. The first term $c_{12}t^{-1/2}(1+k_{12}\overline{\rho}^{n_{10}})$ and the second term $-c_{13}[\overline{f}_{\text{v-}\theta'}/(1-c_{14}\overline{f}_{\text{v}})]^{m_{12}}$ denote the growth rate of the average thickness of θ' precipitate and the influence of dissolution of θ' precipitate on thickness evolution rate, respectively. Similarly, the average thickness of the sheared and non-sheared T_1 precipitates can be expressed as Eqs. (21) and (22), respectively:

$$\dot{S}_{\text{Ts}}=c_{15}t^{-1/2}(1+k_{13}\overline{\rho}^{n_{11}}) \tag{21}$$

$$\dot{S}_{\text{Tns}}=c_{16}t^{-1/2}(1-k_{14}\overline{\rho}^{n_{12}}) \tag{22}$$

where c_{15}, c_{16}, n_{11}, n_{12}, k_{13} and k_{14} are the material-related constants. $\dot{S}_{\text{Ts}}$ and $\dot{S}_{\text{Tns}}$ are the average thickness evolution rates of the sheared and non-sheared T_1 precipitates, respectively. According to abovementioned data and relevant research of HU et al [33], during the CA process, the dislocation density in the material gradually increases as the applied stress increases, which gradually reduces the average thickness of the non-shearable T_1 precipitate. The second item $(1-k_{14}\overline{\rho}^{n_{12}})$ on the right side of Eq. (22) represents the influence of the dislocation on the average length of the non-shearable T_1 precipitate.

4.3 Strengthening models

For heat-treatable strengthening aluminum alloys, the yield strength can be modelled according to a classic law of mixtures, including three strengthening components of precipitation hardening, dislocation hardening and solid solution hardening [17], which can be expressed as

$$\sigma_{\text{y}}=\sigma_{\text{Al}}+\sigma_{\text{ss}}+\sqrt{\sigma_{\text{ppt}}^2+\sigma_{\text{dis}}^2} \tag{23}$$

where σ_{Al} is the aluminum matrix hardening (about 77 MPa), which is determined by the properties of

pure Al and the strengthening contribution originates from grain boundaries. σ_{ss}, σ_{ppt} and σ_{dis} denote the solid solution hardening, the precipitation hardening and the dislocation hardening, respectively.

4.3.1 Solid solution hardening

The solid solution hardening contributions can be represented as a function of the solid atom concentration in the aluminum matrix. Solid solution hardening can be decreased with the nucleation and growth of the precipitates. According to the existing literatures [28,32], it can be expressed

$$\sigma_{ss}=C_S(1-\overline{f}_v)^{m_2} \tag{24}$$

where m_2 and C_S are material constants.

4.3.2 Precipitation hardening

The maximum strength and the hardness of Al−Cu−Li alloys are achieved through the precipitation hardening involving predominantly plate-shaped T_1 and θ' precipitates formed on rational habit planes $\{111\}_\alpha$ and $\{100\}_\alpha$ in α(Al) matrix, respectively [23,34]. θ' precipitate is non-shearable by dislocations with deformation [29]. However, the interaction mechanism of T_1 precipitate and dislocation depends on the thickness of the T_1 precipitate. When the thickness of the T_1 precipitate is less than 3 nm, it can be sheared by dislocations, and it becomes non-shearable when the thickness is larger than 3 nm [35]. Moreover, the hardening contribution of the precipitates is determined by the absolute volume fraction that can be converted from the relative values multiplied by the maximum absolute volume fraction [29]. With the extension of ageing time, θ' precipitate can gradually convert to T_1 precipitate [27]. Moreover, the precipitate in the alloy is mainly T_1 phase. In order to simplify the model, the maximum volume fraction of the precipitate is considered to be approximately equal to that of the T_1 precipitate, and according to previous studies [23,33], the maximum volume fraction f_{max} of T_1 precipitate is approximately 0.27%. It is necessary to analyze the hardening contribution of T_1 and θ' precipitates, respectively. According to the literature [36], the overall precipitate hardening σ_{ppt} is calculated as

$$\sigma_{ppt}=M(\Delta\tau_{Ts}^{1.4}+\Delta\tau_{Tns}^{1.4}+\Delta\tau_{\theta'}^{1.4}) \tag{25}$$

where M is the Taylor factor and its value is 3.331, $\Delta\tau_{\theta'}^{1.4}$ is the hardening contribution of θ' precipitate, $\Delta\tau_{Ts}^{1.4}$ is the hardening contribution of T_1 precipitate which can be sheared by dislocations, $\Delta\tau_{Tns}^{1.4}$ is the hardening contribution of the non-sheared T_1 precipitate. The θ' precipitate tends to be bypassed when interacting with the dislocation during the CA process, and its hardening contribution is calculated with Eq. (26) [34]:

$$\Delta\tau_{\theta'}=\frac{Gb}{2\pi\sqrt{1-v}}\ln(1.225S_{\theta'}/r_i)/[0.931\sqrt{(0.306\pi D_{\theta'}S_{\theta'})/(\overline{f}_{v-\theta'}f_{max})}-\pi D_{\theta'}/8-1.061S_{\theta'}] \tag{26}$$

where G and b denote the shear modulus of the A1 matrix and the magnitude of Burgers vector of the slip dislocations, respectively; v and r_i denote the Poisson ratio and the inner cut-off distance, respectively. It is worth noting that the hardening contribution of the shearable T_1 precipitate is $\Delta\tau_{Ts}$ which can be expressed as [34]

$$\Delta\tau_{Ts}=\frac{1.211D_{Ts}}{S_{Ts}^2}\left(\frac{b\overline{f}_{v\text{-}Ts}f_{max}}{\Gamma}\right)^{1/2}\gamma_i^{3/2} \tag{27}$$

$$\Gamma=(Gb/2\pi)\ln(r_0/r_i) \tag{28}$$

$$r_0=D_{Ts}/\sqrt{2f_{v\text{-}Ts}f_{max}} \tag{29}$$

where γ_i is the interfacial energy between T_1 and the Al matrix, Γ is the dislocation line tension, and r_0 represents the outer cut-off distance. The hardening contribution of non-sheared T_1 phase is $\Delta\tau_{Tns}$, which can be expressed as [34]

$$\Delta\tau_{Tns}=\frac{Gb}{2\pi\sqrt{1-v}}\ln(1.061S_{Tns}/r_0)/[0.931\sqrt{(0.265\pi D_{Tns}S_{Tns})/(\overline{f}_{Tns}f_{max})}-\pi D_{Tns}/8-0.91S_{Tns}] \tag{30}$$

4.3.3 Dislocation hardening

Dislocation hardening is essentially caused by the plastic deformation, which increases with the dislocation density. Many investigations have been conducted to model this phenomenon based on the evolution of the dislocation density [37,38]. Dislocation hardening can be mathematically expressed as

$$\sigma_{dis}=C_{dis}\overline{\rho}^{n_3} \tag{31}$$

where C_{dis} and n_3 are material constants.

4.4 Creep strain−stress correlation

The creep behavior of Al−Li−S4 alloy during the CAF process, which has been studied previously [22,33], demonstrates a novel "multi-stage" creep feature with three creep stages. This new feature is introduced in Section 3.1 and discussed in detail in the study of LI et al [17]. The evolution of three micro-structural parameters, radius of multiple precipitates, dislocation density and solute concentration, contribute to the new "multi-stage" creep feature of the alloy. Therefore, the creep strain−stress correlation is established as

$$\dot{\varepsilon}_{\mathrm{c}}=A\sinh[B(\sigma-\sigma_0)I] \tag{32}$$

$$I=(1+k_1\bar{\rho}^{n_1})(k_0-k^*\bar{C}^{n_2})/(1+k_3D_{\mathrm{Ts}}+k_4D_{\mathrm{Tns}}+k_5D_{\theta'})^{m_1} \tag{33}$$

where A, B, m_1, n_1, n_2, k^*, k_0, k_1, and k_{3-5} are material constants, σ_0 denotes the threshold stress of the alloy during the CA process, and I represents the influence of microstructure variables on creep rate of the alloy, which contains the three micro-structural parameters. The first part $(1+k_1\bar{\rho}^{n_1})$ of I represents the positive effect of mobile dislocation caused by applied stress and creep deformation on creep strain rate. The second part $(k_0-k^*\bar{C}^{n_2})$ shows the influence of the solute concentration on the creep rate, and $-k^*\bar{C}^{n_2}$ represents the negative effect on the creep strain rate. And the last part $(1+k_3D_{\mathrm{Ts}}+k_4D_{\mathrm{Tns}}+k_5D_{\theta'})^{m_1}$ denotes the negative impact of the radius of different kinds of precipitates on the creep rate. During the CA process, microstructure variables influence each other and dominate the "multi-stage" creep feature of the alloy. In Stage I, different kinds of precipitates gradually nucleate and grow up. In addition, due to the applied stress and creep deformation, a large number of dislocations are generated and they reach the saturation level quickly [39], and dislocation strengthening plays a major role at this stage, which makes the creep rate decrease gradually. In Stage II, T_1 and θ' precipitates grow up gradually along the dislocations [21], solute elements in Al matrix continue to be consumed and the dislocation density of the alloy gradually decreases due to dynamic recovery effects of dislocations [17], which makes creep strain increase stably. At the beginning of Stage III, due to the accelerated growth of T_1 and θ' phases, the solute concentration in matrix decreases rapidly, which leads to the decrease of creep resistance [40], and the creep rate increases gradually. As ageing continues, the size and volume fraction of the T_1 precipitate continue to increase, but the θ' precipitate gradually decreases. Besides, the dislocation density and solute concentration tend to stabilize. Combined with the above factors, the creep rate gradually approaches a steady state in Stage III.

According to the previous studies [28,41], the correlation between the relative solute concentration $\bar{C}$ and the relative volume fraction of the precipitate $\bar{f}_{\mathrm{v}}$ can be expressed as

$$\bar{C}=\alpha-\beta\bar{f}_{\mathrm{v}} \tag{34}$$

where α and β are material constants. Therefore, $(k_0-k^*\bar{C}^{n_2})$ can be expressed as

$$k_0-k^*\bar{C}^{n_2}=k_0-k^*(\alpha-\beta\bar{f}_{\mathrm{v}})^{n_2} \tag{35}$$

where k_0 and k^* are material constants. In order to eliminate possible numerical difficulties near $n_2\approx1$, Eq. (35) is transformed to a new form, while keeping its main characteristics shown in Eq. (36):

$$k_0-k^*(\alpha-\beta\bar{f}_{\mathrm{v}})^{n_2}=k_0-k^*\alpha^{n_2}+k^*\beta\bar{f}_{\mathrm{v}}^{n_2}=1+k_2\bar{f}_{\mathrm{v}}^{n_2} \tag{36}$$

where k_2 and n_2 are material constants. Equation (33) transforms to a new form as

$$I=(1+k_1\bar{\rho}^{n_1})(1+k_2\bar{f}_{\mathrm{v}}^{n_2})/(1+k_3D_{\mathrm{Ts}}+k_4D_{\mathrm{Tns}}+k_5D_{\theta'})^{m_1} \tag{37}$$

4.5 Unified creep ageing constitutive model

A new set of unified creep ageing constitutive equations for Al−Li−S4 alloys is established, which is based on the correlation among microstructural variables, strengthening responses and creep strain−stress. The creep ageing constitutive equations can be expressed as follows:

$$\dot{\varepsilon}_{\mathrm{c}}=A\sinh[B(\sigma-\sigma_0)I];$$

$$I=(1+k_1\bar{\rho}^{n_1})(1+k_2\bar{f}_{\mathrm{v}}^{n_2})/(1+k_3D_{\mathrm{Ts}}+k_4D_{\mathrm{Tns}}+k_5D_{\theta'})^{m_1};$$

$$\sigma_{\mathrm{y}}=\sigma_{\mathrm{Al}}+\sigma_{\mathrm{ss}}+\sqrt{\sigma_{\mathrm{ppt}}^2+\sigma_{\mathrm{dis}}^2};$$

$$\sigma_{\mathrm{ss}}=C_{\mathrm{S}}(1-\bar{f}_{\mathrm{v}})^{m_2};$$

$$\sigma_{\text{dis}}=C_{\text{dis}}\bar{\rho}^{n_3};$$

$$\sigma_{\text{ppt}}=M(\Delta\tau_{\text{Ts}}^{1.4}+\Delta\tau_{\text{Tns}}^{1.4}+\Delta\tau_{\theta'}^{1.4});$$

$$\Delta\tau_{\text{Tns}}=\frac{Gb}{2\pi\sqrt{1-v}}\ln(1.061S_{\text{Tns}}/r_0)/[0.931\sqrt{(0.265\pi D_{\text{Tns}}S_{\text{Tns}})/(\bar{f}_{\text{Tns}}f_{\max})}-\pi D_{\text{Tns}}/8-0.91S_{\text{Tns}}];$$

$$\Delta\tau_{\theta'}=\frac{Gb}{2\pi\sqrt{1-v}}[\ln(1.225S_{\theta'}/r_{\text{i}})]/[0.931\sqrt{(0.306\pi D_{\theta'}S_{\theta'})/(\bar{f}_{\text{v-}\theta'}f_{\max})}-\pi D_{\theta'}/8-1.061S_{\theta'}]];$$

$$\Delta\tau_{\text{Ts}}=\frac{1.211D_{\text{Ts}}}{S_{\text{Ts}}^2}\left(\frac{b\bar{f}_{\text{v-Ts}}f_{\max}}{\Gamma}\right)^{1/2}\gamma_i^{3/2};$$

$$\Gamma=(Gb/2\pi)\ln(r_0/r_{\text{i}});$$

$$r_0=D_{\text{Ts}}/\sqrt{2f_{\text{v-Ts}}f_{\max}};$$

$$\bar{f}_{\text{v}}=\bar{f}_{\text{v-}\theta'}+\bar{f}_{\text{v-T}};$$

$$\dot{\bar{f}}_{\text{v-}\theta'}=c_1\dot{D}_{\theta'}D_{\theta'}^2S_{\theta'}(1+k_6\bar{\rho}^{n_4})(1-\bar{f}_{\text{v-}\theta'})^{m_3}-c_2\dot{\bar{f}}_{\text{v-}\theta'}^{m_4};$$

$$\dot{\bar{f}}_{\text{v-Ts}}=c_3\dot{D}_{\text{Ts}}D_{\text{Ts}}^2S_{\text{Ts}}(1+k_7\bar{\rho}^{n_5})(1-\bar{f}_{\text{v-Ts}})^{m_5}+c_4c_2\dot{\bar{f}}_{\text{v-}\theta'}^{m_4}-c_5\dot{\bar{f}}_{\text{v-Ts}}^{m_6};$$

$$\dot{\bar{f}}_{\text{v-Tns}}=[c_5\dot{\bar{f}}_{\text{v-Ts}}^{m_6}+(1-c_4)c_2\dot{\bar{f}}_{\text{v-}\theta'}^{m_4}]\cdot[1+c_6(1+k_8\bar{\rho}^{n_6})(1-\bar{f}_{\text{v-Tns}})^{m_7}];$$

$$\dot{D}_{\theta'}=c_7(Q_1-D_{\theta'})^{m_8}(1+k_9\bar{\rho}^{n_7})-c_8[\bar{f}_{\text{v-}\theta'}/(1-c_9\bar{f}_{\text{v}})]^{m_9};$$

$$\dot{D}_{\text{Ts}}=c_{10}(Q_2-D_{\text{Ts}})^{m_{10}}(1+k_{10}\bar{\rho}^{n_8});$$

$$\dot{D}_{\text{Tns}}=c_{11}(Q_3-D_{\text{Tns}})^{m_{11}}(1-k_{11}\bar{\rho}^{n_9});$$

$$\dot{S}_{\theta'}=c_{12}t^{-1/2}(1+k_{12}\bar{\rho}^{n_{10}})-c_{13}[\bar{f}_{\text{v-}\theta'}/(1-c_{14}\bar{f}_{\text{v}})]^{m_{12}};$$

$$\dot{S}_{\text{Ts}}=c_{15}t^{-1/2}(1+k_{13}\bar{\rho}^{n_{11}});$$

$$\dot{S}_{\text{Tns}}=c_{16}t^{-1/2}(1-k_{14}\bar{\rho}^{n_{12}});$$

$$\bar{\rho}=\bar{\rho}_{\text{i}}+\bar{\rho}_{\text{c}};$$

$$\bar{\rho}_{\text{i}}=\{\rho_0+c_{17}\exp[c_{18}(1+(\sigma-\sigma_{0.2})/\sigma_{0.2})]\}/\rho_{\text{total}};$$

$$\dot{\bar{\rho}}_{\text{c}}=c_{19}(1-\bar{\rho})|\dot{\varepsilon}_{\text{c}}|^{m_{13}}-c_{20}\bar{\rho}^{n_{13}}.$$

4.6 Determination of material constants

The unified creep ageing constitutive equations presented above, containing many unknown material constants, are non-linear ordinary differential equations. Therefore, they are difficult to be solved analytically. It is necessary to decouple the model and fit the parameters step by step. According to previous researches [29,32], particle swarm optimization (PSO), one of the optimization algorithms, has been used to determine the parameters of creep ageing constitutive equations by obtaining the minimum fitness values between experimental data and calculated data. The fitness value is evaluated as

$$f(u)=\sum_{i=1}^{n'}\sum_{j=1}^{m'}w_{\text{c}}\left(u_{ij}^{\text{c}}-u_{ij}^{\text{e}}\right)^2 \tag{38}$$

where u represents the variables to be fitted in the constitutive equation. n' and m' are the numbers of fitted curves and data points on the relevant curves, respectively. i and j represent current fitted curve and current fitted data point on corresponding curve, respectively. w_{c} is a weighting function and $\left(u_{ij}^{\text{c}}-u_{ij}^{\text{e}}\right)^2$ is the difference between the points on the calculated curve and the experimental curve.

It should be indicated that the parameters in the constitutive equation are solved step by step using the optimization algorithm of PSO, and the fitting procedure is as follows. First, the creep strain curves are fitted with polynomials to acquire a function of the creep strain rate. Second, Fig. 8 shows that the material constants correlated to the normalized dislocation density $\bar{\rho}$ (c_{17-20}, m_{13} and n_{13}) are determined using experimental results of the normalized dislocation density evolution with time. Third, based on the fitting parameters of the

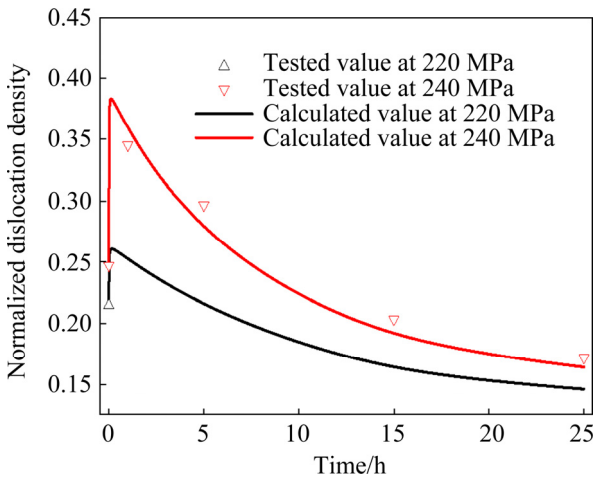

Fig. 8 Predicted evolution of normalized dislocation density during CA process

first and second steps and the experimental results of precipitate size, the material constants correlated to the length and thickness of the T_1 precipitate ($c_{10,11,15,16}$, $k_{10,11,13,14}$, $n_{8,9,11,12}$ and $m_{10,11}$) are determined, as shown in Figs. 9(a_1, a_2, b_1, b_2). Moreover, Figs. 9(c_1, c_2) show that material constants correlated to the length and thickness of θ' precipitate ($c_{7-9,12-14}$, $k_{9,12}$, $n_{7,10}$ and $m_{8,9,12}$) are determined in the same way. Fourth, based on the fitting parameters of the previous three steps and the experimental results of the relative volume fraction of precipitates, the material constants correlated to the relative volume fraction of different precipitates (c_{1-6}, k_{6-8}, n_{4-6} and m_{3-7}) can be obtained, as shown in Fig. 10. Fifth, based on the fitting parameters of the previous four steps and the experimental results of the yield strength during CA process, the remaining constants correlated to yield strength (C_S, C_{dis}, m_2 and n_3) are determined, as shown in Fig. 11. Finally, the rest of constants can be determined, as shown in Fig. 12. Some initial values of variables in the constitutive model are listed in Table 2, and the parameters of the constitutive model are listed in Table 3.

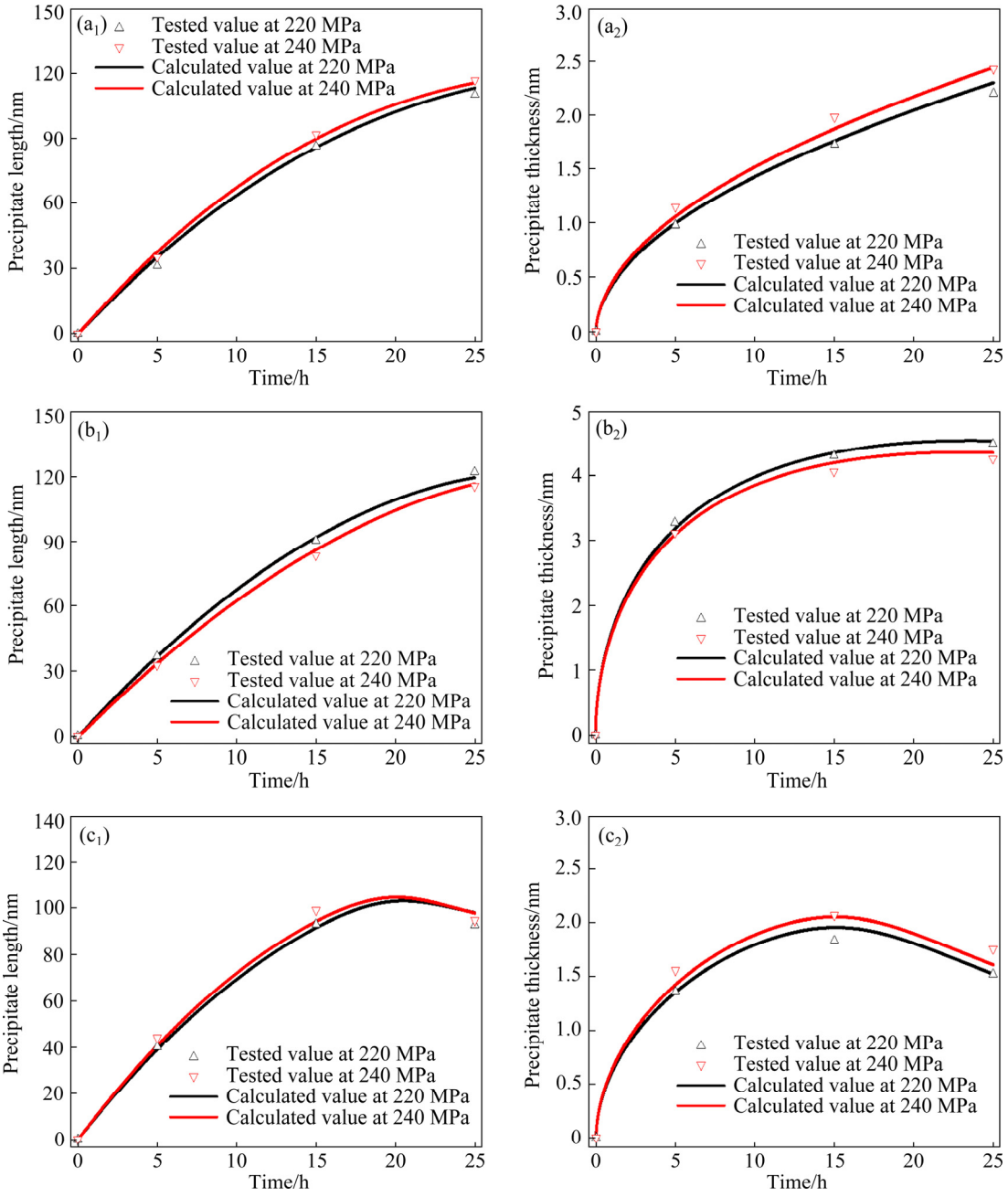

Fig. 9 Comparisons of predicted and experimental average length (a_1, b_1, c_1) and average thickness (a_2, b_2, c_2) of shearable T_1 phase (a_1, b_1) non-shearable T_1 phase (a_2, b_2) and θ' phase (a_3, b_3)

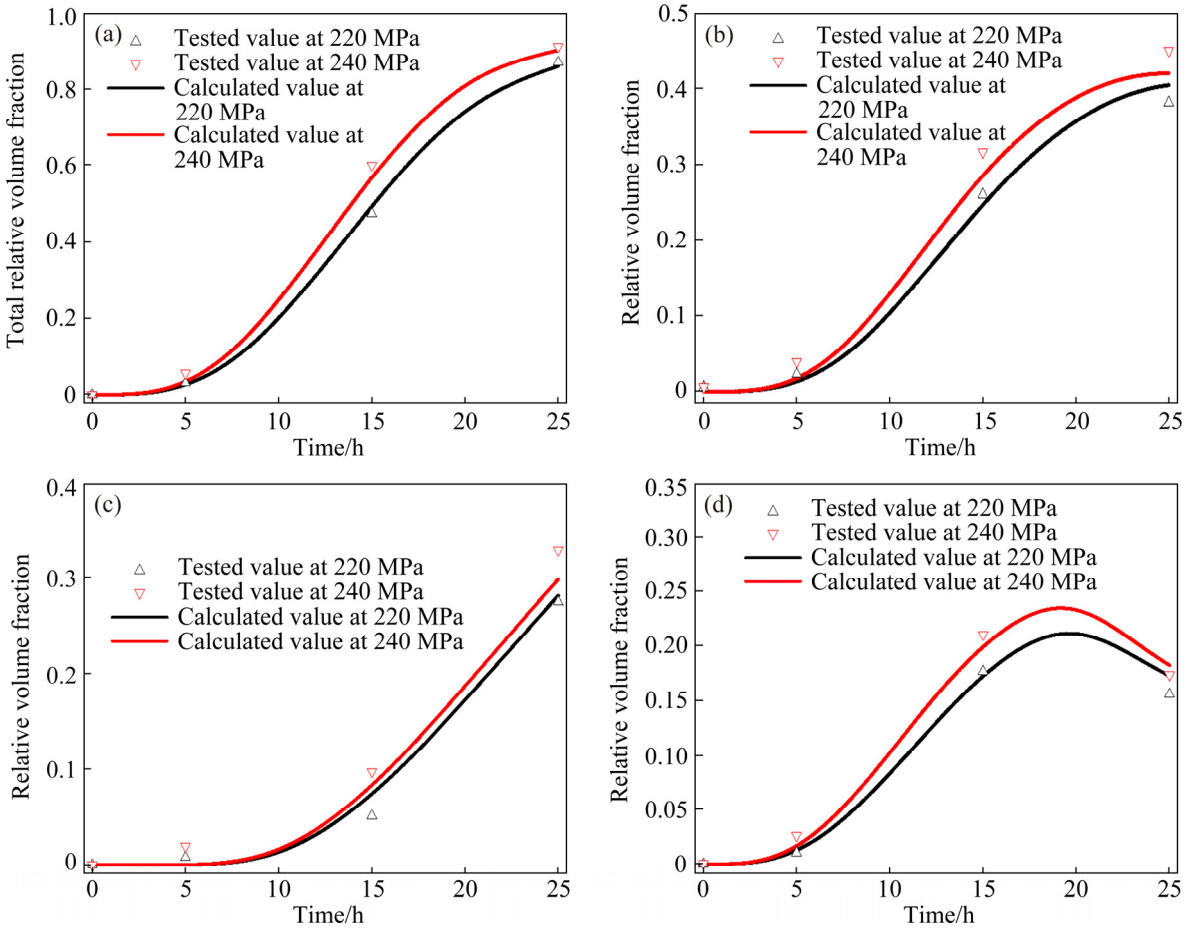

Fig. 10 Comparisons of predicted and experimental results for total relative volume fraction of precipitates (a), relative volume fraction of shearable T_1 phase (b), relative volume fraction of non-shearable T_1 phase (c), and relative volume fraction of θ' phase (d)

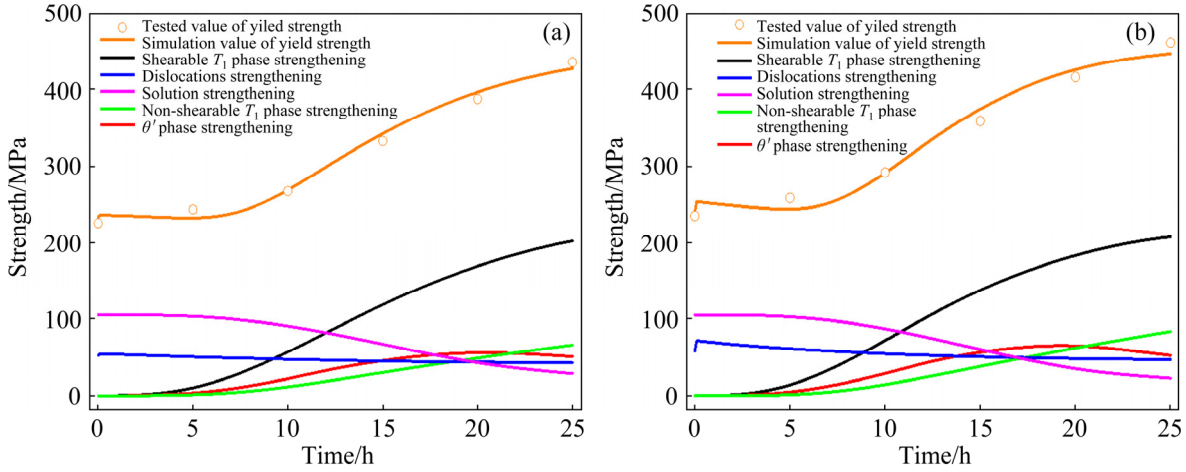

Fig. 11 Evolutions of different hardening mechanisms: (a) 220 MPa; (b) 240 MPa

Table 2 Initial values of variables in constitutive model for Al−Li−S4 alloy

$\overline{\rho}_0$	$\overline{\rho}_{c0}$	$S_{\theta'0}$/nm	S_{Ts0}/nm	S_{Tns0}/nm	$D_{\theta'0}$/nm	D_{Ts0}/nm	D_{Tns0}/nm	$\overline{f}_{v\text{-}\theta'0}$	$\overline{f}_{v\text{-}Ts0}$	$\overline{f}_{v\text{-}Tns0}$
0.202	0	0	0	0	0	0	0	0	0	0

Table 3 Material constants in uniform constitutive equation for creep-ageing of Al−Li−S4 at 153 °C

A	B	C_s/MPa	C_{dis}/MPa	σ_0/MPa	c_1	c_2	c_3	c_4	c_5
1.05×10^{-3}	0.021	105.6	115.2	14.56	5.06×10^{-7}	0.0152	7.1×10^{-7}	0.83	0.10
c_6	c_7	c_8	c_9	c_{10}	c_{11}	c_{12}/h^{-1}	c_{13}	c_{14}	c_{15}/h^{-1}
0.12	0.49	0.25	0.98	0.39	1.38	3.1×10^{-4}	1×10^{-4}	0.9	2.1×10^{-4}
c_{16}/h^{-1}	c_{17}	c_{18}	c_{19}/h^{-1}	c_{20}	n_1	n_2	n_3	n_4	n_5
6.9×10^{-4}	5.5×10^{-4}	5.616	1.83	0.15	0.409	1.15	0.50	0.36	0.18
n_6	n_7	n_8	n_9	n_{10}	n_{11}	n_{12}	n_{13}	m_1	m_2
1.12	1.31	1.42	0.32	0.97	1.58	0.52	2.49	0.673	0.66
m_3	m_4	m_5	m_6	m_7	m_8	m_9	m_{10}	m_{11}	m_{12}
3.32	1.27	1.93	1.82	1.53	0.59	1.25	0.59	0.71	0.40
m_{13}	k_1	k_2	k_3	k_4	k_5	k_6	k_7	k_8	k_9
1.26	1.403	6.89	0.516	0.76	0.422	0.59	1.20	0.2	1.31
k_{10}	k_{11}	k_{12}	k_{13}	k_{14}	Q_1/nm	Q_2/nm	Q_3/nm		
1.80	1.01	0.80	1.89	0.53	104.62	115.78	119.51		

5 Model validation and discussion

5.1 Microstructural evolution

During the CAF process, the evolution of microstructure variables plays a dominant role in the creep rate and mechanical properties of Al−Li−S4 alloys. Figures 8, 9 and 10 show the normalized dislocation density, the average lengths and thicknesses of T_1 and θ' precipitates, and the relative volume fractions of T_1 and θ' precipitates, respectively. In Figs. 9 and 10, the average size and relative volume fraction of shearable T_1 and θ' precipitates increase with the applied stress during the CA process, while the average size of non-shearable T_1 precipitate decreases as the applied stress increases. This is due to a large number of dislocations and vacancies generated under the applied stress above the initial yield strength of the alloy, which can promote the nucleation of T_1 precipitate and make T_1 precipitate more dispersive and finer. Moreover, the average size and relative volume fraction of the θ' precipitate decrease in the later stages of the CA process due to the competitive correlation between θ' precipitate and T_1 precipitate. Furthermore, Figs. 8, 9 and 10 show that the experimental data are consistent with the simulated data by the proposed model. This confirms that the established constitutive model is feasible to characterize creep ageing behavior for Al−Li−S4 alloy.

5.2 Yield strength evolution during CA process

Figure 11 shows the comparisons of the experimental data and calculated results for the evolution of the yield strength and various strengthening contributions, including the dislocation hardening, the precipitation hardening and the solid solution hardening during the CA process. The calculated yield strength curves are consistent with the experimental data in both cases, which verifies the effectiveness of the established model and relevant material parameters in this study. Precipitation strengthening includes sheared T_1 precipitation strengthening, non-sheared T_1 precipitation strengthening and θ' precipitation strengthening. It should be indicated that the strengthening contribution of T_1 precipitate is greater than that of θ' precipitate. Moreover, the strengthening contribution of the sheared T_1 precipitate is greater than that of the non-sheared T_1 precipitate. Furthermore, the evolution law of the strengthening contribution of θ' precipitate is similar to that of its volume fraction, which increases gradually in the early stage of the CA process and decreases gradually in the later stage of CA process. In the early stage of the CA process, dislocation strengthening is the main source of the increase of yield strength, which is the main reason for the different yield strengths under different

applied stresses. The solid solution hardening gradually decreases as the solute atomic concentration decreases during the CA process. The aluminum matrix hardening remains constant during the CA process.

5.3 Creep behavior under different stress levels

Figure 12 shows the comparison of the experimental data and calculated results for the evolution of the creep strains under stress levels from 200 to 240 MPa. It is observed that all predicted creep strain curves are in good agreement with the experimental results during the CA process. The established model and correlated material parameters can not only predict the "multi-stage" creep characteristics of the alloy, but also accurately predict the creep behavior of the alloy under the applied stresses greater or less than the initial yield strength. Therefore, the proposed model can successfully predict the creep strain behavior of Al−Li−S4 alloy.

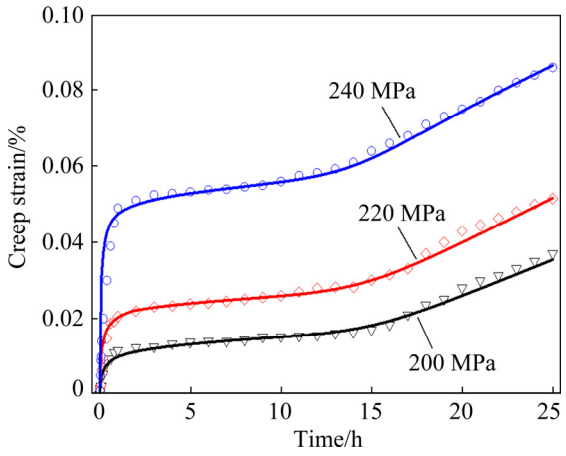

Fig. 12 Comparison of predicted (solid lines) and experimental (symbols) creep-ageing curves of Al−Li−S4 alloy under different stress levels at 153 °C

6 Conclusions

(1) The equations that correlate the yield strength and various strengthening contributions to the microstructural variables of Al−Li−S4 are established according to the basic age hardening model of the Al alloy. The model considers not only the strengthening contributions of sheared and non-sheared T_1 precipitates, but also the strengthening contributions of the θ' precipitate, as well as the strengthening caused by dislocations and solutes. It is observed that the predicted yield strength values are consistent with the experimental data.

(2) The "multi-stage" creep behavior of the Ai−Li−S4 alloy changes slightly under different applied stresses. However, the creep deformation of the alloy in the first stage of the CA process varies significantly. The "multi-stage" creep behavior of Al−Li alloys is mainly determined by the dislocation movement, interaction between dislocation and precipitate, and interaction between solute clusters and dislocations. In this study, a new set of the unified creep ageing constitutive model relating the creep rate to the microstructural variables, including the normalized dislocation density, solute concentration and the average precipitate radius is established under different applied stresses. The model successfully describes the "multi-stage" creep characteristics of Al−Li−S4 alloy, which is in good agreement with the experimental results.

Acknowledgments

The authors are grateful for the financial supports from the National Key R&D Program of China (No. 2017YFB0306300), the National Natural Science Foundation of China (Nos. 51675538, 51601060), the State Key Laboratory of High-performance Complex Manufacturing, China (No. ZZYJKT2018-18), the Fundamental Research Funds for the Central Universities of Central South University, China (No. 2018zzts151).

References

[1] HOLMAN M C. Autoclave age forming large aluminum aircraft panels [J]. Journal of Mechanical Working Technology, 1989, 20: 477−488.

[2] ZHAN Li-hua, LIN Jian-guo, DEAN T A. A review of the development of creep age forming: Experimentation, modelling and applications [J]. International Journal of Machine Tools and Manufacture, 2011, 51(1): 1−17.

[3] ZHAN Li-hua, LI Yan-guang, HUANG Ming-hui. Effects of process parameters on mechanical properties and microstructures of creep aged 2124 aluminum alloy [J]. Transactions of Nonferrous Metals Society of China, 2014, 24(7): 2232−2238.

[4] WAND Qing, ZHAN Li-hua, XU Yong-qian, LIU Chun-hui, ZHAO Xing, XU Ling-zhi, YANG You-liang, CAI Yi-xian. Creep aging behavior of retrogression and re-aged 7150 aluminum alloy [J]. Transactions of Nonferrous Metals Society of China, 2020, 30(10): 2599−2612.

[5] TANG Jian-guo, YU Bo, ZHANG Jin, XU Fu-shun, BAO Chong-jun. Effects of pre-deformation mode and strain on

creep aging bend-forming process of Al−Cu−Li alloy [J]. Transactions of Nonferrous Metals Society of China, 2020, 30(5): 1227−1237.

[6] YANG You-liang, ZHAN Li-hua, LI Jie. Constitutive modeling and springback simulation for 2524 aluminum alloy in creep age forming [J]. Transactions of Nonferrous Metals Society of China, 2015, 25(9): 3048−3055.

[7] RIOJA R J, LIU J. The evolution of Al−Li base products for aerospace and space applications [J]. Metallurgical and Materials Transactions A, 2012, 43(9): 3325−3337.

[8] ELATY A A, XU Yong, ZHANG Shi-hong, MA Yan, CHEN Da-yong. Experimental investigation of tensile properties and anisotropy of 1420, 8090 and 2060 Al−Li alloys sheet undergoing different strain rates and fibre orientation: A comparative study [J]. Procedia Engineering, 2017, 207: 13−18.

[9] GUPTA R K, NAYAN N, NAGASIREESHA G, SHARMA S C. Development and characterization of Al−Li alloys [J]. Materials Science and Engineering A, 2006, 420: 228−234.

[10] DURSUN T, SOUTIS C. Recent developments in advanced aircraft aluminium alloys [J]. Materials and Design, 2014, 56: 862−871.

[11] DECREUS B, DESCHAMPS A, de GEUSER F, DONNADIEU P, SIGLI C, WEYLAND M. The influence of Cu/Li ratio on precipitation in Al−Cu−Li−x alloys [J]. Acta Materialia, 2013, 61(6): 2207−2218.

[12] DESCHAMPS A, DECREUS B, de GEUSER F, DORIN T, WEYLAND M. The influence of precipitation on plastic deformation of Al−Cu−Li alloys [J]. Acta Materialia, 2013, 61(11): 4010−4021.

[13] KOWALEWSKI Z L, HAYHURST D R, DYSON B F. Mechanisms-based creep constitutive equations for an aluminium alloy [J]. The Journal of Strain Analysis for Engineering Design, 1994, 29(4): 309−316.

[14] HO K, LIN Jian-guo, DEAN T A. Constitutive modelling of primary creep for age forming an aluminium alloy [J]. Journal of Materials Processing Technology, 2004, 153−154: 733−751.

[15] LI Chao, WAN Min, WU Xiang-dong, HUANG Lin. Constitutive equations in creep of 7B04 aluminum alloys [J]. Materials Science and Engineering A, 2010, 527: 3623−3629.

[16] ZHAN Li-hua, LIN Jian-guo, DEAN T A, HUANG Ming-hui. Experimental studies and constitutive modelling of the hardening of aluminium alloy 7055 under creep age forming conditions [J]. International Journal of Mechanical Sciences, 2011, 53(8): 595−605.

[17] LI Yong, SHI Zhu-sheng, LIN Jian-guo, YANG Y, RONG Qi, HUANG Bo-ming, CHUNG T F, TSAO C S, YANG J R, BALINT D S. A unified constitutive model for asymmetric tension and compression creep-ageing behaviour of naturally aged Al−Cu−Li alloy [J]. International Journal of Plasticity, 2017, 89: 130−149.

[18] KHAN A S, KAZMI R, PANDEY A V, STOUGHTON T B. Evolution of subsequent yield surfaces and elastic constants with finite plastic deformation. Part-I: A very low work hardening aluminum alloy (Al6061-T6511) [J]. International Journal of Plasticity, 2009, 25(9): 1611−1625.

[19] LEE M G, KIM J H, CHUNG K, KIM S J, WAGONER R H, KIM H. Analytical springback model for lightweight hexagonal close-packed sheet metal [J]. International Journal of Plasticity, 2009, 25(3): 399−419.

[20] LI Yong, SHI Zhu-sheng, LIN Jian-guo, YANG Y, SAILLARD P, SAID R. Effect of machining-induced residual stress on springback of creep age formed AA2050 plates with asymmetric creep-ageing behaviour [J]. International Journal of Machine Tools and Manufacture, 2018, 132: 113−122.

[21] LI Yong, SHI Zhu-sheng, LIN Jian-guo, YANG Y, HUANG Bo-ming, CHUNG T, YANG J R. Experimental investigation of tension and compression creep-ageing behaviour of AA2050 with different initial tempers [J]. Materials Science and Engineering A, 2016, 657: 299−308.

[22] MA Yun-long, XIA Feng, ZHAN Li-hua, XU Yong-qian. Study on multi-step creep aging behavior of Al−Li−S4 alloy [J]. Metals, 2019, 9(7): 807.

[23] RODGERS B, PRANGNELL P B. Quantification of the influence of increased pre-stretching on microstructure−strength relationships in the Al−Cu−Li alloy AA2195 [J]. Acta Materialia, 2016, 108: 55−67.

[24] UNGÁR T, DRAGOMIR I C, REVESZ A, BORBELY A. The contrast factors of dislocations in cubic crystals: The dislocation model of strain anisotropy in practice [J]. Journal of Applied Crystallography, 1999, 32(5): 992−1002.

[25] SIMM T H, WITHERS P J, FONSECA J Q. Peak broadening anisotropy in deformed face-centred cubic and hexagonal close-packed alloys [J]. Journal of Applied Crystallography, 2014, 47(5): 1535−1551.

[26] WILLIAMSON G K, HALL W H. X-ray line broadening from filled aluminium and wolfram [J]. Acta Metallurgica, 1953, 1(1): 22−31.

[27] HUANG Bi-ping, ZHENG Zi-qiao. Precipitation kinetics of an Al−4.01Cu−1.11Li−0.39Mg−0.19Zr−0.11Ti alloy [J]. Scripta Materialia, 1998, 38(4): 611−616.

[28] YANG You-liang, ZHAN Li-hua, SHEN Ru-lin, YIN Xu-ni, LI Xi-cai, LI Wen-ke, HUANG Ming-hui, HE Di-qiu. Effect of pre-deformation on creep age forming of 2219 aluminum alloy: Experimental and constitutive modelling [J]. Materials Science and Engineering A, 2017, 683: 227−235.

[29] MA Zi-yao, ZHAN Li-hua, LIU Chun-hui, XU Ling-zhi, XU Yong-qian, MA Pei-pei, LI Jian-jun. Stress-level-dependency and bimodal precipitation behaviors during creep ageing of Al−Cu alloy: Experiments and modeling [J]. International Journal of Plasticity, 2018, 110: 183−201.

[30] HU Li-bin, ZHAN Li-hua, SHEN Ru-lin, LIU Zhi-lin, MA Zi-yao, LIU Jian, YANG You-liang. Effects of uniaxial creep ageing on the mechanical properties and micro precipitates of Al−Li−S4 alloy [J]. Materials Science and Engineering A, 2017, 688: 272−279.

[31] LIU G, ZHANG Gui-feng, DING Xiang-dong, SUN J, CHEN Kang-hua. Modeling the strengthening response to aging process of heat-treatable aluminum alloys containing plate/disc- or rod/needle-shaped precipitates [J]. Materials Science And Engineering A, 2003, 344: 113−124.

[32] ZHANG Jin, DENG Yun-lai, ZHANG Xin-ming. Constitutive modeling for creep age forming of heat-treatable strengthening aluminum alloys containing

plate or rod shaped precipitates [J]. Materials Science and Engineering A, 2013, 563: 8−15.

[33] HU Li-bin, ZHAN Li-hua, LIU Zhi-lin, SHEN Ru-lin, YANG You-liang, MA Zi-yao, LIU Ming, LIU Jian, YANG Ying-ge, WANG Xun. The effects of pre-deformation on the creep aging behavior and mechanical properties of Al−Li−S4 alloys [J]. Materials Science and Engineering A, 2017, 703: 496−502.

[34] NIE J F, MUDDLE B C. Microstructural design of high-strength aluminum alloys [J]. Journal of Phase Equilibria, 1998, 19(6): 543−551.

[35] SHERCLIFF H R, ASHBY M F. A process model for age hardening of aluminium alloys−II. Applications of the model [J]. Acta Metallurgica et Materialia, 1990, 38(10): 1803−1812.

[36] AHMADI M, POVODENKARADENIZ E, ÖKSÜZ K I, FALAHATI A, KOZESCHNIK E. A model for precipitation strengthening in multi-particle systems [J]. Computational Materials Science, 2014, 91: 173−186.

[37] KOCKS U F. Laws for work-hardening and low-temperature creep [J]. Journal of Engineering Materials and Technology−transactions of the ASME, 1976, 98(1): 76−85.

[38] ESTRIN Y. Dislocation theory based constitutive modelling: Foundations and applications [J]. Journal of Materials Processing Technology, 1998, 80−81: 33−39.

[39] CASSADA W A, SHIFLET G J, STARKE E A. The effect of plastic deformation on $Al_2CuLi(T_1)$ precipitation [J]. Metallurgical Transactions A, 1991, 22(2): 299−306.

[40] SHERBY O D, BURKE P M. Mechanical behavior of crystalline solids at elevated temperature [J]. Progress in Materials Science, 1968, 13: 323−390.

[41] SHERCLIFF H R, ASHBY M F. A process model for age hardening of aluminium alloys−I. The model [J]. Acta Metallurgica et Materialia, 1990, 38(10): 1789−1802.

Al−Li−S4 合金多相析出和多阶段蠕变时效行为的统一本构模型

李 贺[1]，湛利华[1,2,3]，黄明辉[1,2,3]，赵 兴[1,2,3]，周 畅[2]，胡立彬[2]，胡正根[2,4]，刘德博[4]

1. 中南大学 轻合金研究院，长沙 410083；
2. 中南大学 机电工程学院，长沙 410083；
3. 中南大学 高性能复杂制造国家重点实验室，长沙 410083；
4. 北京宇航系统工程研究所，北京 100076

摘 要：提出统一的本构模型，以预测最近观察到的 Al−Li−S4 合金的“多阶段”蠕变行为。通过 X 射线衍射(XRD)和透射电子显微镜(TEM)，详细表征蠕变时效过程中与合金的屈服强度和蠕变变形相关的微观结构变量，包括位错和多种析出相。对于合金的屈服强度，该模型基于强化机制考虑多相强化行为，包括可剪切的 T_1 析出相强化，不可剪切的 T_1 析出相强化和 θ' 析出相强化。基于蠕变变形机理，通过将相互作用的微观结构变量(包括多种析出相的半径，位错密度和溶质浓度)引入蠕变应力应变模型，可以预测合金的“多阶段”蠕变行为。结果表明，模型的计算结果与实验数据吻合良好，验证该模型的有效性。

关键词：本构模型；Al−Li−S4 合金；蠕变时效成形；微观结构；数值算法

(Edited by Bing YANG)